ARTICLE IN PRESS

Nature Communications

https://doi.org/10.1038/s41467-026-71039-1

Article in Press

Epsilon-near-zero time-gate for high-fidelity spatial information transfer through dynamic scattering media

Received: 2 January 2026

Accepted: 12 March 2026

[redacted]

Cite this article as: Xu, Y., Choudhary, S., Nguyen, L.D. *et al.* Epsilon-near-zero time-gate for high-fidelity spatial information transfer through dynamic scattering media. *Nat Commun* (2026). https://doi.org/10.1038/s41467-026-71039-1

Yang Xu, Saumya Choudhary, Long D. Nguyen, Matthew Klein, Shivashankar Vangala, J. Keith Miller, Eric G. Johnson, Joshua R. Hendrickson, M. Zahirul Alam & Robert W. Boyd

We are providing an unedited version of this manuscript to give early access to its findings. Before final publication, the manuscript will undergo further editing. Please note there may be errors present which affect the content, and all legal disclaimers apply.

If this paper is publishing under a Transparent Peer Review model then Peer Review reports will publish with the final article.

ARTICLE IN PRESS

© The Author(s) 2026. **Open Access** This article is licensed under a Creative Commons Attribution-NonCommercial-NoDerivatives 4.0 International License, which permits any non-commercial use, sharing, distribution and reproduction in any medium or format, as long as you give appropriate credit to the original author(s) and the source, provide a link to the Creative Commons licence, and indicate if you modified the licensed material. You do not have permission under this licence to share adapted material derived from this article or parts of it. The images or other third party material in this article are included in the article's Creative Commons licence, unless indicated otherwise in a credit line to the material. If material is not included in the article's Creative Commons licence and your intended use is not permitted by statutory regulation or exceeds the permitted use, you will need to obtain permission directly from the copyright holder. To view a copy of this licence, visit http://creativecommons.org/licenses/by-nc-nd/4.0/.

Epsilon-near-zero time-gate for high-fidelity spatial information transfer through dynamic scattering media

Yang Xu[1*†], Saumya Choudhary[2†], Long D. Nguyen[1],
Matthew Klein[3,4], Shivashankar Vangala[4], J. Keith Miller[5],
Eric G. Johnson[6], Joshua R. Hendrickson[4], M. Zahirul Alam[7],
Robert W. Boyd[1,2,7]

[1*]Department of Physics and Astronomy, University of Rochester, Rochester, 14627, New York, USA.
[2]The Institute of Optics, University of Rochester, Rochester, 14627, New York, USA.
[3]KBR, Beavercreek, 45431, Ohio, USA.
[4]Sensors Directorate, Air Force Research Laboratory, Wright-Patterson AFB, 45433, Ohio, USA.
[5]The Holcombe Department of Electrical and Computer Engineering, Clemson Center for Optical Materials Science and Engineering Technologies, Clemson, 29634, South Carolina, USA.
[6]CREOL, The College of Optics and Photonics at the University of Central Florida, Orlando, 32816, Florida, USA.
[7]Department of Physics, University of Ottawa, Ottawa, K1N 6N5, Ontario, Canada.

*Corresponding author(s). E-mail(s): yxu100@ur.rochester.edu;
†These authors contributed equally to this work.

Abstract

Transparent conducting oxides such as indium-tin-oxide (ITO) exhibit strong optical nonlinearity in the frequency range where their permittivity is near zero. We leverage this nonlinear optical response to realize a sub-picosecond time-gate based on upconversion four-wave mixing (FWM) between two ultrashort pulses centered at the epsilon-near-zero (ENZ) wavelength, in a sub-micron-thick ITO film. By removing the effect of both static and dynamic scattering on the signal pulse, the time gate only retains the photons that are not scattered — the ballistic photons — resulting in high-fidelity transmission of the spatial information encoded in both the intensity and the phase of the signal pulse. Furthermore, in the presence of time-varying scattering, our time-gate can reduce the resulting scintillation by two orders of magnitude. In contrast to traditional bulk nonlinear materials, time gating by sum-FWM in a sub-wavelength-thick ENZ film can produce a scattering-free upconverted signal at a visible wavelength without sacrificing spatial resolution, which is usually limited by the phase matching conditions. Our experiment can have implications for possible applications such as in vivo diagnostic imaging and free-space optical communication.

1 Introduction

Unwanted scattering of light during propagation can severely degrade the quality of the received optical signal, thereby adversely affecting applications such as imaging, sensing, and communication. An ultrafast time-gate can undo the effect of scattering and recover the original unscrambled signal by producing a response only from the unaffected (the “ballistic”) part of the signal. The photons comprising this ballistic signal exit the scattering medium earlier than the other photons as they experience no scattering events. The ability to select/gate only the ballistic photons is of particular importance to many noninvasive biomedical imaging techniques that are primarily limited by light scattering [1–4]. For instance, in transillumination imaging for breast cancer diagnostics, the light scattered by the breast tissue can severely degrade the quality of the shadow image of tumors [5–9]. Previous demonstrations of optical time-gates to retain only ballistic photons have mostly employed the optical Kerr effect [1, 10–14]. In an optical Kerr gate, the nonlinear optical medium is placed between two crossed polarizers. As such, the ballistic part of the signal pulse carrying the image is transmitted only when it spatio-temporally overlaps an intense linearly polarized gate pulse that rotates the polarization of the signal beam. However, even though the nonresonant electronic Kerr response is ultrafast, it is usually weak in most bulk nonlinear optical materials and thus requires long interaction lengths to build up enough rotation of the polarization of the signal beam to produce a sufficient signal-to-noise ratio in the transmitted signal. This long interaction length limits the acceptance angle of the Kerr medium, which constrains the maximum achievable imaging resolution [15]. Hence, despite several experimental attempts to improve the Kerr gating [15–22], simultaneously achieving good image contrast and robustness against strong scattering remains a challenge for traditional Kerr media.

Epsilon-near-zero (ENZ) materials demonstrate exotic linear and nonlinear optical wave phenomena that manifest as a consequence of their vanishing permittivity [23, 24]. In particular, materials have been shown to exhibit a unity-order change in the nonlinear refractive index [25–27], enhanced response for harmonic generation [28–31], frequency conversion [32–34] and wave-mixing [35]. These enhanced nonlinear optical processes have typically been demonstrated on platforms of transparent conducting oxides (TCOs) such as indium-tin-oxide (ITO) or aluminum-doped zinc oxide (AZO).

TCOs are degenerately-doped semiconductors with a large concentration of free electrons leading to permittivities that can be described by the Drude-Lorentz model [36]. Crucially, the nonlinear optical response of these materials has a sub-picosecond time scale due to the electron dynamics in a non-parabolic band structure [36]. This giant ultrafast nonlinearity, together with the tunability of their ENZ regime through doping, makes TCOs ideal platforms for realizing efficient optical switches, as well as ultrafast coherent time-gates to select a part of a signal within a very small (sub-ps) time window [37].

Here, we demonstrate an ultrafast time-gate based on the upconversion four-wave mixing (sum-FWM) process in a sub-wavelength-thick film of ITO [25, 38] for a scattering-free transmission of optical fields through static and dynamic scattering media. We show the preservation of the intensity and phase distributions in the ballistic signal by recovering the spatial structure of an amplitude object and of a beam carrying orbital angular momentum (OAM). The enhanced nonlinearity of ITO under ENZ conditions due to the high field enhancement within the film [26, 39–43] and the relaxation of the phase-matching condition due to its sub-wavelength thickness both help to yield a large sum-FWM signal. Thus, our ENZ time-gate offers a solution to the long-standing trade-off between the strength of the ballistic signal and the spatial resolution. Furthermore, the sum-FWM process, wherein two photons from the gate beam and one photon from the signal beam, all at the near-infrared (NIR) ENZ frequency, upconvert into a signal photon at a visible frequency, enables efficient signal collection with common silicon-based detectors.

2 Results

When a light pulse propagates through a random scattering medium, the photons in the pulse could undergo none or several scattering events before they exit the medium [44, 45]. The spatial and temporal distribution of the field as well as the spatial coherence of the ballistic photons, which experience no scattering events and exit the medium at the earliest, remain unchanged. On the contrary, the diffusive photons, experiencing one or more scattering events, spend a longer time inside the scattering medium, which degrades their temporal coherence [13, 46]. As a consequence of light scattering, the temporal profile of the pulse on exiting the medium, as shown in Fig. 1(a), consists of a small ballistic peak that is an attenuated replica of the incident pulse, followed by a large and broad diffusive component [see Section 1 of Supplementary Information]. Hence, selecting only this ballistic peak through a time-gate should enable the recovery of the original spatial and temporal information carried by the incident signal, except in situations where the scattering is strong enough to deplete the ballistic photons.

We employ the sum-FWM process in a non-collinear geometry involving the ballistic peak of an information-carrying signal pulse and an intense gate pulse [see Fig. 1(b) for an illustration of the concept]. The spatial separation of the gated FWM signal with the scattered signal at the detector guarantees a complete rejection of the scattering background. Both the gate pulse and the unscattered signal pulse are

100-fs-long and centered at a wavelength of 1550 nm, which is close to the ENZ wavelength of the ITO film at 1515 nm [see Supplementary Fig. 4 for the permittivity of the ITO sample]. The wavevectors of the FWM responses obtained from momentum conservation are given by $\boldsymbol{k}_{\mathrm{FWM;\,S}} = 2\boldsymbol{k}_{\mathrm{gate}} + \boldsymbol{k}_{\mathrm{signal}}$ for the sum-FWM signal at the frequency $\omega_{\mathrm{FWM;\,S}} = 2\omega_{\mathrm{gate}} + \omega_{\mathrm{signal}}$ [see Supplementary Fig. 5 for the energy level diagrams of all possible FWM processes that occur in ITO]. Thus, the sum-FWM signal is centered at a wavelength of 517 nm (or the frequency-triple of the gate and the signal pulses) and is emitted at a small transverse angle. The smaller emission angle also reduces its spatial walk-off with the gate and signal pulses and potential resolution loss in imaging. In addition, from the expressions of the nonlinear polarization for the FWM process, we note that the sum signal [$P_{\mathrm{NL,FWM;S}} = 3\epsilon_0\chi^{(3)}\boldsymbol{E}^2_{\mathrm{gate}}\boldsymbol{E}_{\mathrm{signal}}$] is directly proportional to the signal field itself, which further justifies our use of the sum-FWM response to recover the spatial information carried by the signal field.

2.1 Upconversion imaging through scattering media

We first demonstrate the use of our time-gate for the upconversion imaging of an amplitude-only object through strong static scattering media. The test object is a the group 2, element 2 set of horizontal bars with a resolution of 4.49 lp/mm on a negative USAF 1951 resolution target [see Supplementary Fig. 2(a)]. The width of each bar, as well as the spacing between two adjacent bars is ≈ 111 μm. We position the scatterer directly after the object in the path of the signal pulse. The amplitude images of the unscattered signal field [Fig. 2(a)] and the sum-FWM field [Fig. 2(b)], respectively, along with their corresponding line cuts [Fig. 2(c)–(d)] are collected and measured on a camera. We note that the sum-FWM image is nearly 4× smaller than the direct image of the object in the signal field for two reasons: (1) the sum-FWM field at the Fourier plane is linearly proportional to the signal field but with its wavelength reduced by a third, which accordingly scales the field in the image plane [see Section 2.2 in the Supplementary Information for further explanation], and (2) the collimating lens in the path of the signal (sum-FWM) pulse has a focal length of 50 (40) mm, which further adds a factor of 1.25× in the difference in magnification.

We first use a set of two 2-mm-thick ground glass optical diffusers with grit numbers of 1500 and 600 as the static scatterers. From the bidirectional scattering distribution function (BSDF) shown in Supplementary Fig. 2(b) that characterizes the scattering strength of the diffusers, we note that the outgoing light scattered by the 600-grit ground glass optical diffuser has a wider angular distribution, thereby indicating a stronger scattering effect. The direct images of the signal field in Figs. 3(a)–(c), and the corresponding images of the sum-FWM field with the 1500-grit diffuser, the 600-grit diffuser, and the 1500- plus 600-grit diffusers combination, respectively are presented in Figs. 3(g)–(i). The associated line cuts along the dashed white line [Figs. 3(d)–(f) and 3(j)–(l)] in the direct images [Figs. 3(a)–(c)] and the sum-FWM images [Figs. 3(g)–(i)] characterize the signal-to-noise contrast. We varied the power of the signal pulse for the different diffusers to overcome the corresponding power extinction and to maintain similar exposure times on the CMOS camera used to capture the sum-FWM images. Increasing the scattering strength of the diffuser leads to a progressive degradation of the image quality in the scattered signal to the extent that the object becomes indiscernible when the two diffusers are combined. In contrast, the structure of the object stays well preserved in the sum-FWM image for all three scattering strengths, and the generated sum-FWM field is bright enough for a commercially available CMOS camera (Thorlabs Zelux 1.6 MP monochrome CMOS camera) to detect. The difference in quality between the scattered signal and the sum-FWM images is more evident in the respective line cuts, wherein the features of the object are completely submerged by the scattering noise in panels (b) and (c), whereas a marginal difference between panels (g), (h) and (i) is present for the sum-FWM image.

We quantify the image quality for the various scatterers considered using the peak signal-to-noise ratio (PSNR) [47] and the Pearson correlation coefficient (PCC) [48]. PSNR is a common metric to quantify the strength of the obscuring noise that affects the image quality [49, 50]. PCC gives a linear correlation between the pixel array of the reference image and the pixel array of the examined image and is often used to describe the similarity of the patterns in two images (see Methods). Table 1 shows the PSNR and PCC metrics of the direct images of the scattered signal and sum-FWM images for the various diffusers considered. We use the signal image [Fig. 2(c)] and sum-FWM image [Fig. 2(e)] taken without any scatterer as the reference images to exclude the effects of aberrations and the intensity profile of the illuminating signal beam. We note from Table 1 that the PSNR drops by 6.47 dB, and the PCC is reduced by a factor of 4 for the signal image from the lowest to the highest scattering strength, whereas both metrics remain mostly constant for the sum-FWM image. We note that the slightly higher PSNR of the sum-FWM image for the 600-grit diffuser could be attributed to a relatively higher signal power, which was set by a visual inspection of the sum-FWM image contrast, leading to a slightly brighter sum-FWM image than for the other two diffusers. These metrics align with the result in Fig. 3(c) where the object is completely obscured in the signal image for the highest scattering strength but remains intact in the sum-FWM image in Fig. 3(i).

2.2 Transmission of phase structures through scattering media

The recovery of the underlying signal by time gating the ballistic photons applies not only to its amplitude but also to its phase. Hence, we show that the phase distribution of a spatially structured beam, specifically a beam carrying an orbital angular momentum (OAM) [51, 52], is also well preserved in the gated sum-FWM field even in the presence of relatively strong scattering. In recent years, the OAM of light has become a promising candidate for free-space quantum communication [53] because of its high information capacity [54] and its compatibility with other degrees of freedom, such as polarization [55]. However, turbulence in free-space links inevitably leads to strong intermodal crosstalk that severely distorts the received signal [56, 57]. Therefore, the transfer of OAM through turbulent media with high fidelity is a crucial step in the development of robust OAM-based free-space communication protocols [58, 59].

In this demonstration (see Methods), we swap the imaging system in the path of the signal pulse with a spiral phase plate that introduces an OAM of topological charge $l = 2$ in the signal beam. The generated sum-FWM field is given by

$$E_{\mathrm{FWM;\,S}}(\mathbf{r}, 2\omega_{\mathrm{gate}} + \omega_{\mathrm{signal}}) \propto \left[E_{\mathrm{gate}}(\mathbf{r}, \omega_{\mathrm{gate}})\right]^2 E_l(\mathbf{r}, \omega_{\mathrm{signal}}), \tag{1}$$

where $E_{\mathrm{gate}}(\mathbf{r}, \omega_{\mathrm{gate}})$ is approximately Gaussian. $E_l(\mathbf{r}, \omega_{\mathrm{signal}})$ is the signal field after the spiral phase plate and carries a topological charge $l = 2$ [60], so the sum-FWM field $E_{\mathrm{FWM;S}}(\mathbf{r}, 2\omega_{\mathrm{gate}})$ should have the same OAM as the signal field $E_l(\mathbf{r}, \omega_{\mathrm{signal}})$.

We compare the spatial profiles of the signal field with those of the sum-FWM field without and with the 600-grit and 1500-grit ground glass diffusers combined in Fig. 4. In Fig. 4(b), we note that scattering due to diffusers adds noise to the spatial profile of the signal, but its donut shape remains preserved, along with its topological charge, as shown by the cylindrical lens transform [Figs. 4(c) and (d)] [61]. However, for the sum-FWM field, both the transverse spatial profile [Figs. 4(e) and (f)] and the topological charge [Figs. 4(g) and (h)] show robustness to scattering. Table 2 shows the PSNR of the scattered signal and the sum-FWM for all the diffusers considered. The corresponding images of the scattered signal field and the gated sum-FWM field are presented in Supplementary Fig. 9. As before, we calculate the PSNR from the spatial profiles of the scattered signal field and the sum-FWM field with their respective profiles in the absence of scattering used as references. As the scattering strength increases, the PSNR of the scattered signal field drops from 20.31 dB to 15.27 dB. On the other hand, the PSNR of the sum-FWM field remains stable around 20 dB. Specifically, for the 600-grit diffuser and the combined diffuser stack (600-grit plus 1500-grit), a 4-dB difference in PSNR between the scattered signal field and the sum-FWM field shows an excellent rejection of scattering by the time-gate.

2.3 Real-time removal of scattering

Real scattering media, such as a cloud cover or biological tissues, are dynamic, as the light-scattering particles are in constant Brownian motion. Therefore, the real-time removal of scattering and scintillation is an important factor to consider in the design of any imaging or optical communication modality in such systems. In this section, we show that our time-gate is also highly effective in removing the scintillation from dynamic or time-varying scattering media.

In the first study, we use polystyrene beads of average diameters of 7.7 μm suspended in an aqueous solution as the dynamic scattering medium. This suspension is contained in a 2-mm-thick glass cuvette and placed after the object in the path of the signal pulse. The bead suspension functions as an excellent time-varying scattering medium because of the Brownian motion of the beads in water and is often used in biomedical imaging to mimic light scattering in biological tissues. Table 3 compares the image quality metrics (PSNR and PCC) of the frozen frames of the scattered signal with the gated sum-FWM image at various bead concentrations. Similar to the results in Table 1, both metrics of the sum-FWM images remain much higher than the direct images for all bead concentrations considered. The frozen frames of the scattered signal, and the gated sum-FWM images at various bead concentrations are shown in Supplementary Fig. 10.

To quantify the performance of our time-gate for dynamic scattering media, we monitor the intensity fluctuations of the scattered signal and gated sum-FWM images over a fixed period of time. These results [Supplementary Movies 1 and 2] show that the image quality of the sum-FWM field remains stable within a 10-second time interval, whereas the signal field shows a strong scintillation effect as a consequence of the random motion of beads. To quantify these intensity fluctuations, or "scintillation", we define the scintillation index σ_s at each pixel as

$$\sigma_s = \frac{\left\langle I^2 \right\rangle}{\left\langle I \right\rangle^2} - 1, \tag{2}$$

where $\langle\cdot\rangle$ denotes the time average. We uniformly split the 10-second video into 200 frames and calculate the scintillation index for each pixel in similar regions of interest for both signal and sum-FWM images. The resultant scintillation index map thus indicates the stability of the image in a dynamic scattering medium.

As shown in Figs. 5(a) and 5(b), the scintillation maps of the direct images of the USAF resolution test target in the path of the signal pulse, and of the scattering-free upconverted sum-FWM images at a bead concentration of 0.525 g/cm^3 characterize the performance of our ITO time gate in a time-varying scattering medium. The corresponding results for the lower bead concentrations are shown in Supplementary Figs. 11(a) and (b). We note that the scintillation map of the signal images [Fig. 5(a)] shows large pixel-to-pixel variation in σ_s in contrast to the scintillation index map for the sum-FWM images [Fig. 5(b)], which has almost negligibly small values of σ_s throughout. Hence, the scattered signal field has large intensity fluctuations over time, whereas the gated sum-FWM field is essentially a static image with all the artifacts due to scattering removed. As such, the histograms of σ_s for the signal field [Figs. 5(c) and Fig. 5(d)] show a much wider distribution than for the corresponding sum-FWM field [Figs. 5(g) and Fig. 5(h)] with values that are approximately two orders of magnitude larger.

In the second study of the OAM transfer through scattering media, we slowly rotate the ground glass diffusers and monitor the scintillation in the spatial profile of the OAM-encoded signal field. The variation of the intensity profiles of the scattered signal field and the gated sum-FWM field as the combined diffuser stack (1500-grit and 600-grit) is rotated is shown in Supplementary Movie 3, and the respective scintillation maps and the associated histogram counts in Figs. 5(e)-(h). We measure an order of magnitude larger overall values of σ_s with a wider distribution in this instance compared to the latex beads for the signal field. In contrast, we measure negligible scintillation for the gated sum-FWM field. In both studies, the larger values of σ_s are obviously concentrated in the regions of intensity minima of the original fields as σ_s is normalized to the time-averaged intensity, which is homogenized over the fluctuations and approaches the original unscattered intensity distributions. The corresponding results for the 1500-grit and the 600-grit diffusers are shown in Supplementary Figs. 11(c) and (d).

3 Discussion

Besides ultrafast time-gating, optical coherence tomography (OCT) [62–64] is another powerful tool for imaging structures within biological tissues by coherence-gating ballistic photons. The use of a low temporally-coherent broadband NIR light source in OCT enables this gating, allowing depth-resolved high-resolution imaging up to 1–2 mm into the scattering media. However, the residual scattering effect from multiply scattered photons and the (static or dynamic) refractive index variations in the scattering media affects the stability of this interferometric scheme, and could contribute to significant image degradation. Ballistic gating schemes, on the contrary, are more robust against such deleterious effects. OCT also cannot be used with transparent or highly absorbing samples that have very little backscattered photons available for interferometry. Additionally, it does not have the wavelength conversion functionality due to being a purely linear effect. The sum-FWM process in our implementation of the time gate upconverts the frequency of the image-carrying beam into the visible region, thereby enabling easier photon detection through efficient silicon-based detectors over InGaAs [65]. We note that phase-matching is difficult to achieve for sum-FWM in most bulk media due to dispersion and is not an efficient process. Sum-FWM has previously been reported in systems with a very short interaction length, such as dielectric metasurfaces [66], highly focused beams in gases and atomic vapor [67–69], and in an ENZ film [37]. The tunability of the ENZ wavelength of TCOs through doping and by integrating with metasurfaces [27], also provides tremendous flexibility to customize the gate for the wavelength of choice. Furthermore, our gating technique could be extended to materials that have an ENZ wavelength at mid-IR frequencies such as doped semiconductors like CdO [70] and polar dielectrics [71], which would enable the upconversion of ballistic mid-IR photons to recover images at visible or near-infrared (NIR) wavelengths. The mid-IR imaging and sensing through scattering media is essential in chemical sensing [72], non-destructive biomedical imaging [73], and detection of explosives [74] but is particularly limited by the lack of sensitive and fast detectors.

In addition, we compare the performance of our time gate with two other established time-gating methods in supplementary Table S1. The traditional Kerr gate uses a CS_2 cell as the nonlinear medium [1, 11, 13], which along with the instantaneous electronic nonlinearity [75], also has a slower nonlinearity due to molecular orientation [76]. Consequently, the actual width of the time gate can reach more than 500 fs (FWHM) for a 100-fs incident gating pulse [75, 77]. In contrast to this Kerr-type gating in ITO, a non-negligible sum-FWM signal can only be generated for a strictly non-negligible temporal overlap between the gate pulse and the signal pulse. Thus the generated sum-FWM signal is not affected by the longer recovery time of ITO and consequently only limited by the pulse width of the gate pulse. Other time gates based on second- or third-order nonlinear processes in bulk crystals such as sum/difference frequency generation (SFG/DFG) [16, 78–80], third-order harmonic cross correlation [81], and difference-FWM [82] have also been shown to increase the signal-to-noise ratio and the brightness of the signal. These modalities based on fast electronic responses do reduce the width of the gate to that of the incident pulse and also enable frequency conversion. However, the tight focusing of the image-carrying beam inside the bulk crystals used in either Kerr gating or SFG/DFG gating leads to a loss of resolution given the limited acceptance angle of the nonlinear crystal due to phase matching condition [80]. In this context, our sub-wavelength-thick ENZ film with a large nonlinearity generates an efficient gated signal with a complete rejection of scattering and no loss of spatial resolution. Further, our ENZ time gating method outperforms traditional upconversion gating methods using bulk nonlinear crystals since strong nonlinearity at ENZ wavelength enables the simultaneous use of a thin nonlinear material and a large effective aperture size determined by the width of the pump beam [see Section S5 in the Supplementary Information for further discussion]. In our experiment, we measured the modulation transfer function (MTF) values ≈ 0.85 for three chosen targets with spatial resolutions of 4.49, 8.00 and 10.10 lp/mm (or 111, 62.5 and 49.6 μm line widths), respectively, which far exceeds the demonstrated resolution limit for gating with a bulk KDP crystal [80], or a PPLN crystal [73].

We also note that our ENZ time-gating method based on the third-order nonlinearity of ITO should outperform both Kerr gate and SFG/SHG gate in terms of the pulse transmission factor [83, 84], which describes the sensitivity to the minimal incident signal pulse and is useful in the characterization of strong scattering media [81]. Based on the similarity of the underlying nonlinear processes, the transmission factor of our ENZ-based sum-FWM gate should match that of the latest third-order cross-correlation method (10^{-12}) [81] because the nonlinear conversion efficiency of both methods scale with the square of the gate intensity. On the other hand, the conversion efficiency of SHG/SFG processes and the nonlinear refractive index change in the optical Kerr gating scale linearly with the intensity of the gate pulse [76]. The higher-order intensity dependence of the third-order nonlinearity makes our method inherently much more sensitive to pulse transmission than these other third-order nonlinear optical counterparts.

Finally, the past advancement in light-guiding through complex media using computational wavefront shaping methods [85, 86] have shown great adaptability to various scattering conditions. We expect that our optics-based upconversion time-gating method can alleviate the computational overhead of these aforementioned methods by pre-selecting the quasi-ballistic photons. We also note that due to pump-induced anisotropy of the ENZ-enhanced nonlinear response in an ITO film [25], recovering information encoded in a polarization structured signal beam through our gating technique would require a similarly polarization structured gate beam along with an ENZ-based metasurface [87]. We will address this full-vectorial field recovery through scattering media in future work.

In conclusion, we have demonstrated a nonlinear optical transfer of spatial information encoded in both intensity and phase through scattering media along with upconversion using the enhanced instantaneous third-order nonlinear response of ITO in the ENZ regime. The sub-picosecond nonlinear response and the large field enhancement in ENZ materials make them an excellent platform for transmitting signals through static or time-varying scattering media. Furthermore, the efficient upconversion FWM process in our gate enables signal recovery at visible wavelengths without compromising the imaging resolution or the rapid temporal response. The use of a sub-wavelength-thick ITO film and the compatibility of our detection scheme with silicon-based detectors have greatly improved the compactness of this ballistic gating scheme and opened up new avenues for signal recovery through complex media. Finally, we have studied the robustness of our time gate with respect to time-varying scattering media and have shown an excellent rejection of scintillation, thereby allowing real-time retrieval of signal with high fidelity. This dynamic gating of ballistic photons is highly relevant for both underwater and free-space optical communication, and for non-invasive *in vivo* biomedical imaging.

4 Methods

4.1 Experimental setup

The schematic of our setup for the sum-FWM time-gate is shown in Supplementary Fig. 6 with panel (a) showing the configuration for recovering images, and panel (b) the configuration for the transfer of OAM. In both setups, the OPA (Coherent OPerA Solo) produces our 100 fs-wide source pulse centered at 1550 nm with a repetition rate of 1 kHz. The source pulse is split evenly into gate and signal pulses. The energy of the gate pulse is held fixed at 22 μJ. The signal beam then passes through the (a) object (spiral phase plate) followed by the scattering medium and is then focused by a plano-convex lens (f = 20 mm, NA = 0.23) onto the ITO sample from the side of the substrate. The overall axial resolution of the imaging system is limited by the NA of this focusing lens, which is given by $\frac{2\lambda}{\mathrm{NA}^2} \approx 19.55\ \mu m$ for the sum-FWM image. The gate pulse goes through a delay stage, which controls the relative optical path delay between the gate and the signal pulses, and is gently focused to a point behind the thin-film ITO by a lens with a longer focal length (f = 300 mm). The different focusing lenses for the gate pulse and signal pulse yield a focal spot of the gate beam that is approximately 7× larger than the signal. The reason for this much larger spot size of the gate beam is two-fold: (i) we need to ensure an efficient nonlinear conversion from the tails of the angular spectrum of the signal when the object is in place to preserve the imaging resolution; (ii) a large enough local transverse spatial profile of the incident Gaussian gate beam within the ITO film ensures a mostly uniform intensity of the gate beam over the signal field, thereby minimizing any additional amplitude modulation of the gated sum-FWM field. The sum-FWM is collected on a CMOS camera (Thorlabs CS165MU) with or without an imaging lens for configurations (a) and (b), respectively. The signal is also similarly collected on a stabilized NIR camera (Xenics Bobcat 640) with or without an imaging lens. The intensities of the gate and the signal fields without any scatterers were 70.5 GW/cm^2 and 184.1 GW/cm^2, respectively. We adjust the temporal delay between the gate pulse and the scattered signal pulse to overlap with the early-arriving ballistic photons. For the different combinations of ground glass diffusers, the energy of the incident signal pulse is set to 2 μJ (no scattering), 8.2 μJ (1500-grit), 23 μJ (600-grit), and 28.6 μJ (600-grit + 1500-grit) before the USAF target to account for the increased extinction. The generated sum-FWM field is completely free from any scattering and is also bright enough to be collected by the CMOS camera. We place the scatterers right after the object or the phase plate in configurations (a) and (b), respectively.

4.2 Calculation of the peak signal-to-noise ratio (PSNR) and the Pearson correlation coefficient (PCC)

Peak signal-to-noise ratio (PSNR) is a commonly used metric for image quality, and is given by the ratio of the maximum power of the signal and the power of the distorting noise. The PSNR of a given image can be calculated from the following expression

$$\mathrm{PSNR} = 20\log_{10}\left(\frac{R}{\sqrt{\mathrm{MSE}}}\right) \tag{3}$$

where R is the maximum signal power in the reference image and MSE is the mean squared error defined as

$$\mathrm{MSE} = \frac{1}{MN}\sum_{i=1}^{M}\sum_{j=1}^{N}\left|x_{ij} - y_{ij}\right|^2 . \tag{4}$$

Here, x_{ij} (y_{ij}) stands for the gray-scale value of the pixel at the i^{th} row and j^{th} column of the $M \times N$ tested (reference) image.

The Pearson correlation coefficient (PCC) is also a computational metric for describing the similarity between two images and is given by the linear correlation between the pixel arrays of the two images. PCC is mostly used in image processing for pattern recognition and image classification, and can be calculated from the following expression

$$\mathrm{PCC} = \frac{\sum_i (x_i - x_m)(y_i - y_m)}{\sqrt{\sum_i (x_i - x_m)^2}\sqrt{\sum_i (y_i - y_m)^2}} . \tag{5}$$

Here x_i (y_i) is the intensity of the i^{th} pixel in the first (second) image, and x_m (y_m) is the mean intensity of all pixels in the first (second) image. The value of PCC ranges from -1 to 1. A PCC of 1 (-1) shows that the pixels in the two images are completely correlated (anti-correlated). In our calculations, all images are read in 8-bit gray-level format and centered and cropped to the same size prior to computing both metrics.

Data Availability

Source Data file has been deposited in Figshare under accession code DOI link [88].

Acknowledgements

This work is supported by the U.S. Office of Naval Research (N00014-19-1-2247, MURI N00014-20-2558). R.W.B. acknowledges funding from the Natural Sciences and Engineering Research Council of Canada, the Canada Research Chairs program, and the Canada First Research Excellence Fund. J.R.H. acknowledges support from the Air Force Office of Scientific Research under Grant No. FA9550-25RYCOR006.

Author Contributions

M.Z.A. and R.W.B. conceived the idea of this study. Y.X. and S.C. designed and performed the experiment with the assistance of L.D.N. M.K., S.V. and J.R.H. fabricated the ITO samples used in the experiment. J.K.M. and E.G.J. produced the phase plate used for OAM generation. Y.X. and S.C. analyzed the data. Y.X., S.C. and M.Z.A. wrote the manuscript with input from all authors. R.W.B. supervised the project.

Competing Interests

The authors declare no competing interests.

Tables

Table 1 Peak signal-to-noise ratio (PSNR) and Pearson correlation coefficient (PCC) of the scattered signal images and the upconverted four-wave-mixing (sum-FWM) images for different ground glass diffusers.

	Scattered Signal at 1550 nm		Sum-FWM at 517 nm	
Scattering Medium	PSNR (dB)	PCC	PSNR (dB)	PCC
1500-grit ground glass	16.25	0.887	24.61	0.940
600-grit ground glass	10.54	0.373	27.77	0.962
600-grit & 1500-grit	9.78	0.219	24.77	0.940

Table 2 Peak signal-to-noise ratio (PSNR) of the transverse spatial profile of the signal field carrying $l = 2$ and the corresponding upconverted four-wave-mixing (sum-FWM) field.

Scattering Medium	Scattered Signal PSNR (dB)	Sum-FWM PSNR (dB)
1500-grit	20.31	20.64
600-grit	15.87	19.74
600-grit & 1500-grit	15.27	19.27

Table 3 Peak signal-to-noise ratio (PSNR) and Pearson correlation coefficient (PCC) of the direct images and the upconverted four-wave-mixing (sum-FWM) images of the USAF target for latex beads suspension with different mass concentrations.

	Scattered Signal at 1550 nm		Sum-FWM at 517 nm	
Latex Bead Concentration (g/cm^3)	PSNR (dB)	PCC	PSNR (dB)	PCC
0.175	15.85	0.878	20.36	0.976
0.350	15.28	0.856	21.64	0.920
0.525	15.24	0.850	20.78	0.961

Figure Captions

Figure 1: Concept of ballistic photons and time gated imaging method. (a) Diagram illustrating the ballistic and diffusive parts of the scattered pulse. A 100-fs-wide incident pulse experiences multiple scattering inside a medium. The ballistic portion of the pulse (blue) retains the shape of the incident pulse, while the diffusive photons constitute the elongated pulse (purple) that follows the ballistic peak. (b) The configuration of gate pulse and the scattered signal pulse for realizing the four-wave mixing gate. The sum-FWM (drawn in green) is generated at the third-harmonic or $3\omega_{\text{signal}}$ of the signal frequency ω_{signal}. (c) The normalized power P of the sum-FWM signal at a wavelength of 517 nm as a function of the time delay τ between the gate and the signal pulses. The FWM response is essentially the autocorrelation between two 100-fs-wide Gaussian pulses, which demonstrates the fast nonlinear response associated with FWM in ITO. The shaded green regions represent the standard deviation in (normalized) measured power.

Figure 2: Direct infrared imaging and four-wave mixing imaging of a USAF 1951 resolution test target. (a) The direct NIR image of the target and (c) its line cut along the white dashed line in the signal field without any scattering medium in place. (b) The corresponding image and (d) its line cut profile of the sum-FWM field. The line cut of the undistorted signal image is rescaled to the same size as the FWM signal for comparing imaging quality. The green colormap has been used in the sum-FWM image for clarity.

Figure 3: Direct imaging and time gated imaging through static scattering media. Direct images of the signal field with diffusers of grit numbers of (a) 1500, (b) 600, and (c) 1500 and 600 combined. The panels (d–f) show the corresponding line cuts (solid, blue) along the white dashed line. The line cut of the undistorted signal image is overlaid for comparison. The panels (g–i) show the images of the sum-FWM field for the signal images in panels (a–c) respectively, and the corresponding line cuts (j–l) along the dashed white line. The line cut of the unscattered signal image rescaled to the magnification of the CMOS sensor (dashed, orange) is overlaid for comparison. Both the image resolution and the signal-to-noise contrast are well preserved in the sum-FWM output.

Figure 4: Transfer of orbital angular momentum of light through scattering media with four-wave mixing on ITO. (a), (b) Spatial profiles of the incident signal field carrying an OAM of $l = 2$ with no scatterer and with the combined (1500- and 600-grit) ground glass diffusers. (c), (d) The corresponding profiles at the focus of a cylindrical lens. (e), (f) Spatial profiles of the sum-FWM field and (g), (h) the corresponding profiles at the focus of a cylindrical lens with no scatterer and with the combined diffusers. The spatial profiles at the focus of the cylindrical lens show that the topological charge of the signal and the sum-FWM fields are largely robust to scattering effects.

Figure 5: Real-time suppression of time-varying scattering effect. Scintillation index maps of the USAF target in the (a) direct image of the scattered signal, and in the (b) gated sum-FWM image. The nearly uniformly black plot shows that the scintillation index is everywhere nearly vanishing. The associated normalized histogram counts are shown in (c) and (d). The scattering medium is the aqueous

suspension of moving latex beads with a mass concentration of 0.525 g/cm^3. The scintillation effect due to dynamic light scattering is suppressed by two orders of magnitude in the sum-FWM image. (e–h) Scintillation index maps and the associated histogram counts of the OAM-encoded signal field and the sum-FWM field. The dynamic scatterer is created by rotating the combined ground glass diffusers (1500-grit and 600-grit). The gated sum-FWM field shows minimal intensity fluctuations despite a strong scattering of the incident signal field. The scintillation index of each pixel is computed from 200 frames taken within 10 seconds.

References

[1] Wang, L., Ho, P., Liu, C., Zhang, G. & Alfano, R. Ballistic 2-d imaging through scattering walls using an ultrafast optical kerr gate. *Science* **253**, 769–771 (1991).

[2] Linne, M., Paciaroni, M., Hall, T. & Parker, T. Ballistic imaging of the near field in a diesel spray. *Experiments in Fluids* **40**, 836–846 (2006).

[3] Paciaroni, M. & Linne, M. Single-shot, two-dimensional ballistic imaging through scattering media. *Applied Optics* **43**, 5100–5109 (2004).

[4] Ipus, E., Bravo-Medina, B. & Strojnik, M. Scope of using ballistic photons for applications in biological tissue (2019).

[5] Bartrum Jr, R. J. & Crow, H. C. Transillumination lightscanning to diagnose breast cancer: a feasibility study. *American Journal of Roentgenology* **142**, 409–414 (1984).

[6] Sickles, E. A. Breast cancer detection with transillumination and mammography. *American Journal of Roentgenology* **142**, 841–844 (1984).

[7] Geslien, G. E., JR, F. & DeLaney, C. Transillumination in breast cancer detection: screening failures and potential. *American Journal of Roentgenology* **144**, 619–622 (1985).

[8] Cutler, M. Transillumination of the breast. *Annals of Surgery* **93**, 223–234 (1931).

[9] Merritt, C. R., Sullivan, M. A., Segaloff, A. & McKinnon, W. P. Real-time transillumination light scanning of the breast. *Radiographics* **4**, 989–1009 (1984).

[10] Duguay, M. & Hansen, J.-W. An ultrafast light gate. *Applied Physics Letters* **15**, 192–194 (1969).

[11] Wang, L., Ho, P. P. & Alfano, R. Time-resolved fourier spectrum and imaging in highly scattering media. *Applied Optics* **32**, 5043–5048 (1993).

[12] Das, B., Yoo, K. & Alfano, R. Ultrafast time-gated imaging in thick tissues: a step toward optical mammography. *Optics Letters* **18**, 1092–1094 (1993).

[13] Alfano, R., Liang, X., Wang, L. & Ho, P. Time-resolved imaging of translucent droplets in highly scattering turbid media. *Science* **264**, 1913–1915 (1994).

[14] d'Abzac, F.-X., Kervella, M., Hespel, L. & Dartigalongue, T. Experimental and numerical analysis of ballistic and scattered light using femtosecond optical kerr gating: a way for the characterization of strongly scattering media. *Optics Express* **20**, 9604–9615 (2012).

[15] Huang, Z. *et al.* High-transmittance femtosecond optical kerr gate with double gate pulses based on birefringence effect (2022).

[16] Yoo, K., Xing, Q. & Alfano, R. Imaging objects hidden in highly scattering media using femtosecond second-harmonic-generation cross-correlation time gating. *Optics Letters* **16**, 1019–1021 (1991).

[17] Sedarsky, D., Berrocal, E. & Linne, M. Quantitative image contrast enhancement in time-gated transillumination of scattering media. *Optics Express* **19**, 1866–1883 (2011).

[18] Zheng, Y., Tan, W., Liu, X. & Tong, J. Ballistic imaging through an intense scattering medium using a supercontinuum with a roundabout spatial gate. *Optics Express* **25**, 20431–20436 (2017).

[19] Mathieu, F., Reddemann, M. A., Palmer, J. & Kneer, R. Time-gated ballistic imaging using a large aperture switching beam. *Optics Express* **22**, 7058–7074 (2014).

[20] Zhan, P. *et al.* Optical imaging of objects in turbid media using heterodyned optical kerr gate. *Applied Physics Letters* **104** (2014).

[21] Tan, W. *et al.* High contrast ballistic imaging using femtosecond optical kerr gate of tellurite glass. *Optics Express* **21**, 7740–7747 (2013).

[22] Tan, W. *et al.* Sharpness-enhanced ultrafast imaging by using a biased optical kerr gate. *Optics Express* **22**, 28100–28108 (2014).

[23] Liberal, I. & Engheta, N. Near-zero refractive index photonics. *Nature Photonics* **11**, 149–158 (2017).

[24] Reshef, O., De Leon, I., Alam, M. Z. & Boyd, R. W. Nonlinear optical effects in epsilon-near-zero media. *Nature Reviews Materials* **4**, 535–551 (2019).

[25] Alam, M. Z., De Leon, I. & Boyd, R. W. Large optical nonlinearity of indium tin oxide in its epsilon-near-zero region. *Science* **352**, 795–797 (2016).

[26] Caspani, L. *et al.* Enhanced nonlinear refractive index in ε-near-zero materials. *Physical Review Letters* **116**, 233901 (2016).

[27] Alam, M. Z., Schulz, S. A., Upham, J., De Leon, I. & Boyd, R. W. Large optical nonlinearity of nanoantennas coupled to an epsilon-near-zero material. *Nature Photonics* **12**, 79–83 (2018).

[28] Wang, W. *et al.* Second harmonic generation investigation of indium tin oxide thin films. *Thin Solid Films* **365**, 116–118 (2000).

[29] Capretti, A., Wang, Y., Engheta, N. & Dal Negro, L. Enhanced third-harmonic generation in si-compatible epsilon-near-zero indium tin oxide nanolayers. *Optics Letters* **40**, 1500–1503 (2015).

[30] Capretti, A., Wang, Y., Engheta, N. & Dal Negro, L. Comparative study of second-harmonic generation from epsilon-near-zero indium tin oxide and titanium nitride nanolayers excited in the near-infrared spectral range. *ACS Photonics* **2**, 1584–1591 (2015).

[31] Yang, Y. *et al.* High-harmonic generation from an epsilon-near-zero material. *Nature Physics* **15**, 1022–1026 (2019).

[32] Zhou, Y. *et al.* Broadband frequency translation through time refraction in an epsilon-near-zero material. *Nature Communications* **11**, 2180 (2020).

[33] Pang, K. *et al.* Adiabatic frequency conversion using a time-varying epsilon-near-zero metasurface. *Nano Letters* **21**, 5907–5913 (2021).

[34] Liu, C. *et al.* Photon acceleration using a time-varying epsilon-near-zero metasurface. *ACS Photonics* **8**, 716–720 (2021).

[35] Carnemolla, E. G. *et al.* Visible photon generation via four-wave mixing in near-infrared near-zero-index thin films. *Optics Letters* **46**, 5433–5436 (2021).

[36] Khurgin, J. B., Clerici, M. & Kinsey, N. Fast and slow nonlinearities in epsilon-near-zero materials. *Laser & Photonics Reviews* **15**, 2000291 (2021).

[37] Jaffray, W. *et al.* Near-zero-index ultra-fast pulse characterization. *Nature Communications* **13**, 3536 (2022).

[38] Naik, G. V., Kim, J. & Boltasseva, A. Oxides and nitrides as alternative plasmonic materials in the optical range. *Optical Materials Express* **1**, 1090–1099 (2011).

[39] Reshef, O. *et al.* Beyond the perturbative description of the nonlinear optical response of low-index materials. *Optics Letters* **42**, 3225–3228 (2017).

[40] Campione, S., de Ceglia, D., Vincenti, M. A., Scalora, M. & Capolino, F. Electric field enhancement in ϵ-near-zero slabs under tm-polarized oblique incidence. *Physical Review B—Condensed Matter and Materials Physics* **87**, 035120 (2013).

[41] Kaipurath, R. *et al.* Optically induced metal-to-dielectric transition in epsilon-near-zero metamaterials. *Scientific Reports* **6**, 27700 (2016).

[42] Lee, Y. U. *et al.* Strong nonlinear optical response in the visible spectral range with epsilon-near-zero organic thin films. *Advanced Optical Materials* **6**, 1701400 (2018).

[43] Vassant, S., Hugonin, J.-P., Marquier, F. & Greffet, J.-J. Berreman mode and epsilon near zero mode. *Optics Express* **20**, 23971–23977 (2012).

[44] Jönsson, J. & Berrocal, E. Multi-scattering software: part i: online accelerated monte carlo simulation of light transport through scattering media. *Optics Express* **28**, 37612–37638 (2020).

[45] Frantz, D., Jönsson, J. & Berrocal, E. Multi-scattering software part ii: experimental validation for the light intensity distribution. *Optics Express* **30**, 1261–1279 (2022).

[46] Pierrat, R., Greffet, J.-J., Carminati, R. & Elaloufi, R. Spatial coherence in strongly scattering media. *JOSA A* **22**, 2329–2337 (2005).

[47] Korhonen, J. & You, J. Peak signal-to-noise ratio revisited: Is simple beautiful? (2012).

[48] Cohen, I. *et al.* Pearson correlation coefficient. *Noise Reduction in Speech Processing* 1–4 (2009).

[49] Yuanji, W., Jianhua, L., Yi, L., Yao, F. & Qinzhong, J. Image quality evaluation based on image weighted separating block peak signal to noise ratio (2003).

[50] Poobathy, D. & Chezian, R. M. Edge detection operators: Peak signal to noise ratio based comparison. *IJ Image, Graphics and Signal Processing* **10**, 55–61 (2014).

[51] Yao, A. M. & Padgett, M. J. Orbital angular momentum: origins, behavior and applications. *Advances in Optics and Photonics* **3**, 161–204 (2011).

[52] Mair, A., Vaziri, A., Weihs, G. & Zeilinger, A. Entanglement of the orbital angular momentum states of photons. *Nature* **412**, 313–316 (2001).

[53] Willner, A. E., Pang, K., Song, H., Zou, K. & Zhou, H. Orbital angular momentum of light for communications. *Applied Physics Reviews* **8** (2021).

[54] Pang, K. *et al.* Demonstration of a 10 mbit/s quantum communication link by encoding data on two laguerre–gaussian modes with different radial indices. *Optics Letters* **43**, 5639–5642 (2018).

[55] Nemirovsky-Levy, L., Pereg, U. & Segev, M. Increasing quantum communication rates using hyperentangled photonic states. *Optica Quantum* **2**, 165–172 (2024).

[56] Zhou, Y. *et al.* High-fidelity spatial mode transmission through a 1-km-long multimode fiber via vectorial time reversal. *Nature Communications* **12**, 1866 (2021).

[57] Hamadou Ibrahim, A., Roux, F. S., McLaren, M., Konrad, T. & Forbes, A. Orbital-angular-momentum entanglement in turbulence. *Physical Review A—Atomic, Molecular, and Optical Physics* **88**, 012312 (2013).

[58] Li, S., Chen, S., Gao, C., Willner, A. E. & Wang, J. Atmospheric turbulence compensation in orbital angular momentum communications: Advances and perspectives. *Optics Communications* **408**, 68–81 (2018).

[59] Li, J. *et al.* Mitigation of atmospheric turbulence with random light carrying oam. *Optics Communications* **446**, 178–185 (2019).

[60] Kotlyar, V. V. *et al.* Generation of phase singularity through diffracting a plane or gaussian beam by a spiral phase plate. *JOSA A* **22**, 849–861 (2005).

[61] Alperin, S. N., Niederriter, R. D., Gopinath, J. T. & Siemens, M. E. Quantitative measurement of the orbital angular momentum of light with a single, stationary lens. *Optics Letters* **41**, 5019–5022 (2016).

[62] Huang, D. *et al.* Optical coherence tomography. *Science* **254**, 1178–1181 (1991).

[63] Fujimoto, J. G. *et al.* Optical biopsy and imaging using optical coherence tomography (1995).

[64] Fercher, A. F. Optical coherence tomography. *Journal of Biomedical Optics* **1**, 157–173 (1996).

[65] Barh, A., Rodrigo, P. J., Meng, L., Pedersen, C. & Tidemand-Lichtenberg, P. Parametric upconversion imaging and its applications. *Advances in Optics and Photonics* **11**, 952–1019 (2019).

[66] Liu, S. *et al.* An all-dielectric metasurface as a broadband optical frequency mixer. *Nature communications* **9**, 2507 (2018).

[67] Wallace, S. C. & Zdasiuk, G. High-efficiency four-wave sum mixing in magnesium at 140 nm. *Applied Physics Letters* **28**, 449–451 (1976).

[68] Hilber, G., Lago, A. & Wallenstein, R. Broadly tunable vacuum-ultraviolet/extreme-ultraviolet radiation generated by resonant third-order frequency conversion in krypton. *JOSA B* **4**, 1753–1764 (1987).

[69] Hodgson, R., Sorokin, P. & Wynne, J. J. Tunable coherent vacuum-ultraviolet generation in atomic vapors. *Physical Review Letters* **32**, 343 (1974).

[70] Runnerstrom, E. L. *et al.* Polaritonic hybrid-epsilon-near-zero modes: beating the plasmonic confinement vs propagation-length trade-off with doped cadmium oxide bilayers. *Nano Letters* **19**, 948–957 (2018).

[71] Passler, N. C. *et al.* Strong coupling of epsilon-near-zero phonon polaritons in polar dielectric heterostructures. *Nano Letters* **18**, 4285–4292 (2018).

[72] Christ, S. & Schäferling, M. Chemical sensing and imaging based on photon upconverting nano-and microcrystals: a review. *Methods and Applications in Fluorescence* **3**, 034004 (2015).

[73] Zhang, H., Kumar, S., Sua, Y. M., Zhu, S. & Huang, Y.-P. Near-infrared 3d imaging with upconversion detection. *Photonics Research* **10**, 2760–2767 (2022).

[74] Ma, Y. & Wang, L. Upconversion luminescence nanosensor for tnt selective and label-free quantification in the mixture of nitroaromatic explosives. *Talanta* **120**, 100–105 (2014).

[75] Yan, L., Yue, J., Si, J. & Hou, X. Influence of self-diffraction effect on femtosecond pump-probe optical kerr measurements. *Optics Express* **16**, 12069–12074 (2008).

[76] Boyd, R. W. *Nonlinear Optics* (Academic Press, 2020).

[77] Tong, J. *et al.* Femtosecond optical kerr effect measurement using supercontinuum for eliminating the nonlinear coherent coupling effect. *Journal of Optics* **14**, 045203 (2012).

[78] Watson, J., Georges, P., Lépine, T., Alonzi, B. & Brun, A. Imaging in diffuse media with ultrafast degenerate optical parametric amplification. *Optics Letters* **20**, 231–233 (1995).

[79] Andreoni, A., Bondani, M., Potenza, M. A. & Villani, F. Viewing'objects hidden in highly scattering media by cross-correlating the fourier transform of the image with the incident field in a second-order non-linear crystal. *Optics Communications* **174**, 487–497 (2000).

[80] Faris, G. W. & Banks, M. Upconverting time gate for imaging through highly scattering media. *Optics Letters* **19**, 1813–1815 (1994).

[81] Bocoum, M., Cheng, Z., Kaur, J. & Lopez-Martens, R. Third-order nonlinear femtosecond optical gating through highly scattering media. *Physical Review A* **106**, L051501 (2022).

[82] Sappey, A. D. Optical imaging through turbid media with a degenerate four wave mixing correlation time gate. *Applied Optics* **33**, 8346–8354 (1994).

[83] Tong, J. *et al.* Measurements of the scattering coefficients of intralipid solutions by a femtosecond optical kerr gate. *Optical Engineering* **50**, 043607–043607 (2011).

[84] Calba, C., Méès, L., Rozé, C. & Girasole, T. Ultrashort pulse propagation through a strongly scattering medium: simulation and experiments. *JOSA A* **25**, 1541–1550 (2008).

[85] Mididoddi, C. K. *et al.* Threading light through dynamic complex media. *Nature Photonics* 1–7 (2025).

[86] Haim, O., Boger-Lombard, J. & Katz, O. Image-guided computational holographic wavefront shaping. *Nature Photonics* **19**, 44–53 (2025).

[87] Karimi, M. *et al.* Interactions of fundamental mie modes with thin epsilon-near-zero substrates. *Nano Letters* **23**, 11555–11561 (2023).

[88] Xu, Y. *et al.* https://doi.org/10.6084/m9.figshare.28780994 (2025).

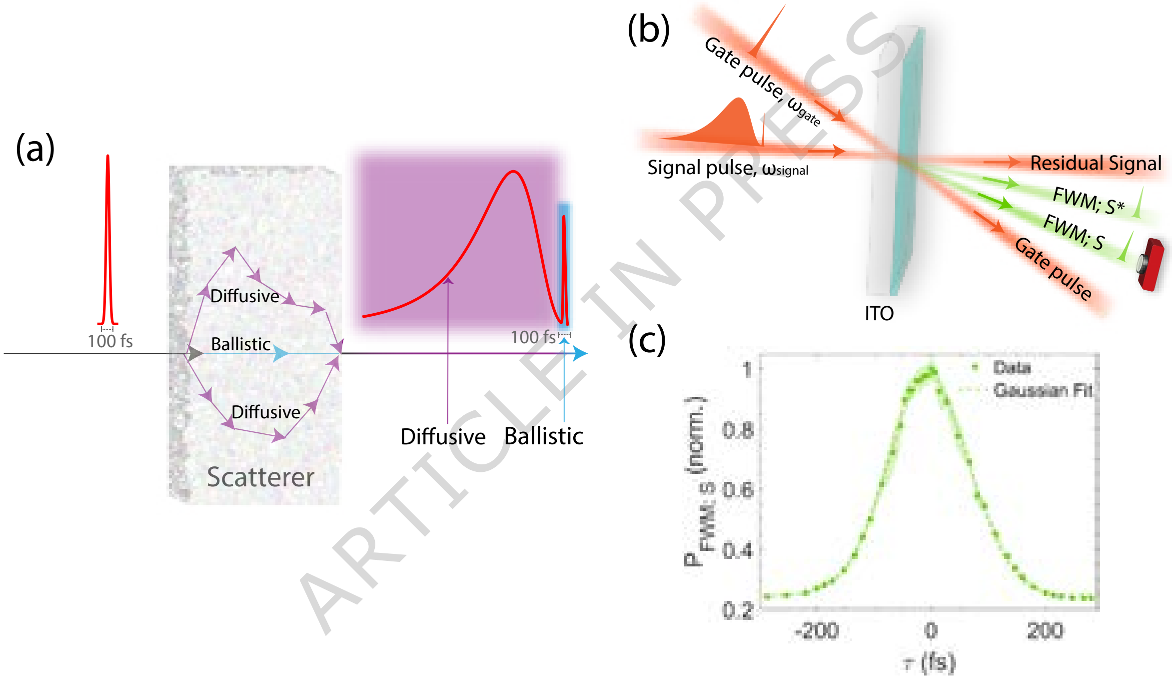
(a)
100 fs
Diffusive
Ballistic
Diffusive
Scatterer
100 fs
Diffusive
Ballistic
(b)
Gate pulse, ω_{gate}
Signal pulse, ω_{signal}
Residual Signal
FWM; S*
FWM; S
Gate pulse
ITO
(c)
Data
Gaussian Fit
$P_{FWM; S}$ (norm.)
1
0.8
0.6
0.4
0.2
-200
0
200
τ (fs)

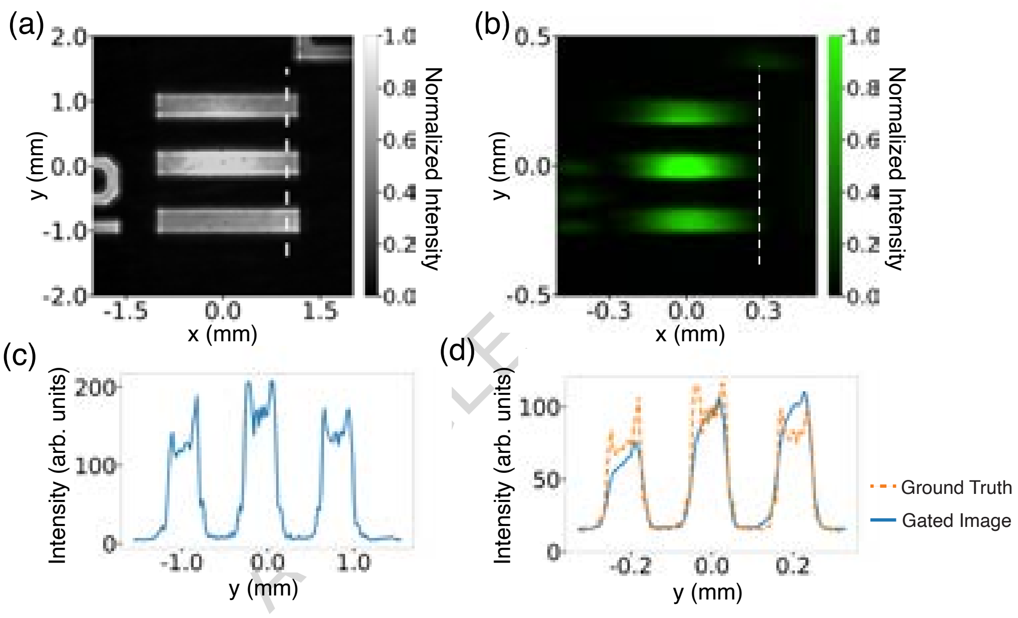
(a)
y (mm)
2.0
1.0
0.0
-1.0
-2.0
-1.5
0.0
1.5
x (mm)
1.0
0.8
0.6
0.4
0.2
0.0
Normalized Intensity
(b)
y (mm)
0.5
0.0
-0.5
-0.3
0.0
0.3
x (mm)
1.0
0.8
0.6
0.4
0.2
0.0
Normalized Intensity
(c)
Intensity (arb. units)
200
100
0
-1.0
0.0
1.0
y (mm)
(d)
Intensity (arb. units)
100
50
0
-0.2
0.0
0.2
y (mm)
Ground Truth
Gated Image

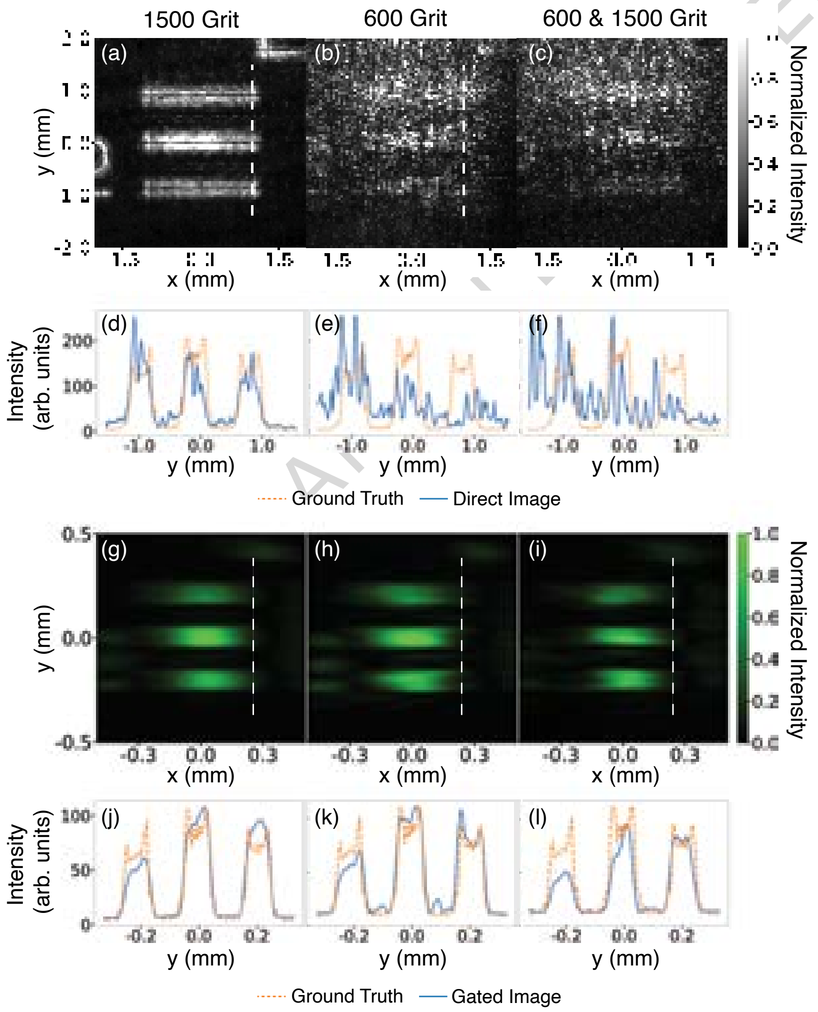
1500 Grit
600 Grit
600 & 1500 Grit
(a)
(b)
(c)
y (mm)
-2.0
1.5
1.5
1.5
1.5
x (mm)
x (mm)
x (mm)
Normalized Intensity
(d)
(e)
(f)
Intensity (arb. units)
200
100
0
-1.0
0.0
1.0
y (mm)
y (mm)
y (mm)
Ground Truth
Direct Image
(g)
(h)
(i)
y (mm)
0.5
0.0
-0.5
-0.3
0.0
0.3
x (mm)
x (mm)
x (mm)
Normalized Intensity
0.8
0.6
0.4
0.2
0.0
(j)
(k)
(l)
Intensity (arb. units)
100
50
0
-0.2
0.0
0.2
y (mm)
y (mm)
y (mm)
Ground Truth
Gated Image

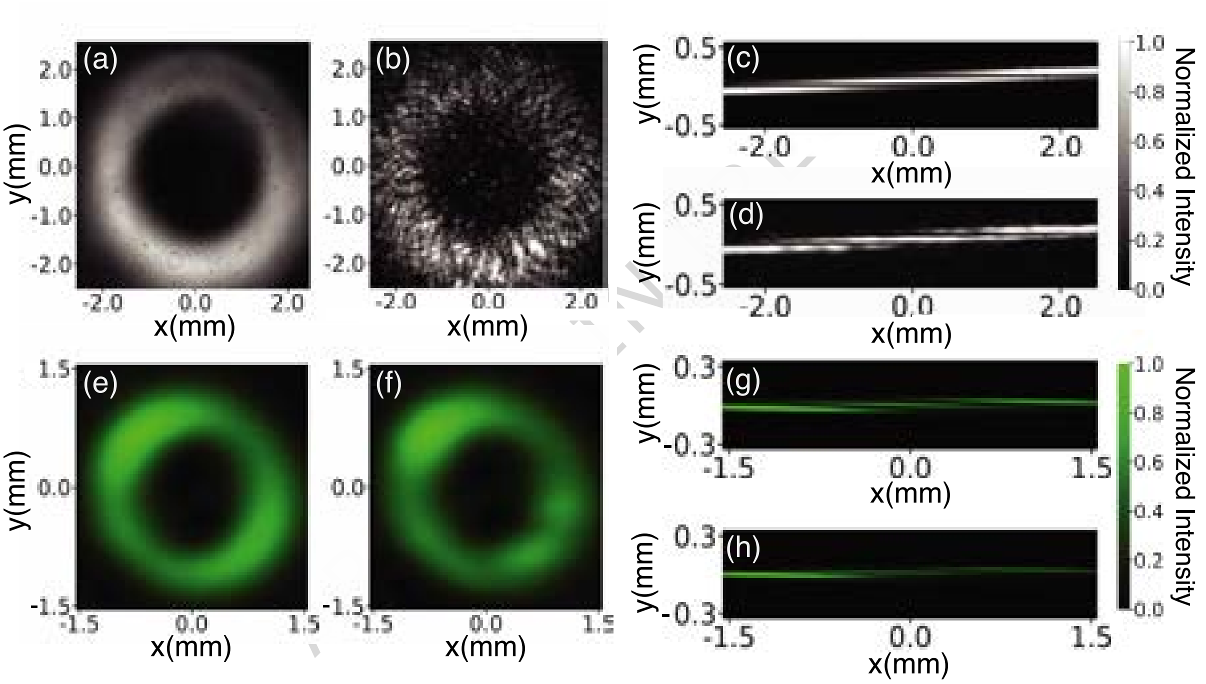
(a)
(b)
(c)
(d)
(e)
(f)
(g)
(h)
y(mm)
x(mm)
2.0
1.0
0.0
-1.0
-2.0
0.5
-0.5
1.5
-1.5
0.3
-0.3
Normalized Intensity
1.0
0.8
0.6
0.4
0.2
0.0

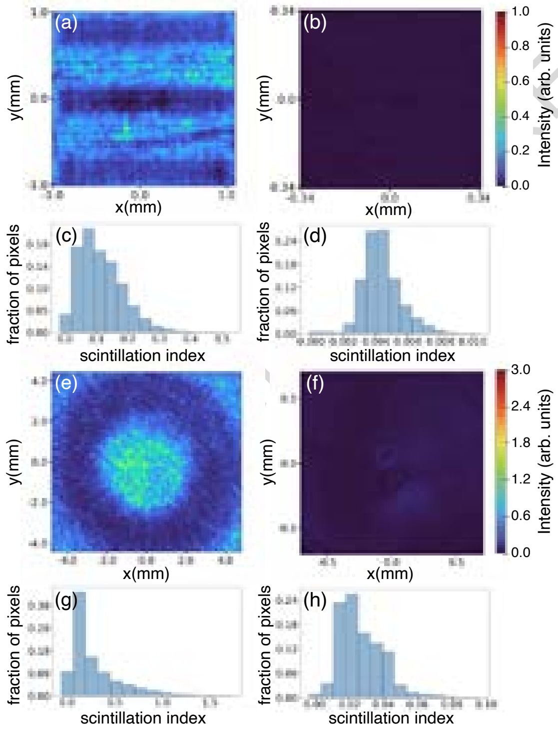
(a)
y(mm)
x(mm)
(b)
y(mm)
x(mm)
1.0
0.8
0.6
0.4
0.2
0.0
Intensity (arb. units)
(c)
fraction of pixels
scintillation index
(d)
fraction of pixels
scintillation index
(e)
y(mm)
x(mm)
(f)
y(mm)
x(mm)
3.0
2.4
1.8
1.2
0.6
0.0
Intensity (arb. units)
(g)
fraction of pixels
scintillation index
(h)
fraction of pixels
scintillation index